Full Paper

CONTRAST MEDIA & MOLECULAR IMAGING

Received: 12 February 2013, Revised: 15 April 2013, Accepted: 06 May 2013, Published online in Wiley Online Library

(wileyonlinelibrary.com) DOI: 10.1002/cmmi.1548

In vivo near-infrared fluorescence targeting of T cells: comparison of nanobodies and conventional monoclonal antibodies

Peter Bannas[a]*†, Lennart Well[a,b†], Alexander Lenz[a,b], Björn Rissiek[b], Friedrich Haag[b], Joanna Schmid[a,b], Katja Hochgräfe[c], Martin Trepel[d], Gerhard Adam[a], Harald Ittrich[a] and Friedrich Koch-Nolte[b]

The large size of conventional antibodies impedes tissue penetration and renal elimination, resulting in suboptimal *in vivo* targeting. Here we assess the utility of nanobodies and nanobody-Fc-fusion proteins as alternatives to monoclonal antibodies as theranostics, using T cell ADP–ribosyltransferase 2 (ART2) as a model antigen for specific targeting of lymph nodes. ART2-specific monovalent nanobody s + 16a (17 kDa), a bivalent Fc-fusion protein of s + 16a (s + 16-mFc, 82 kDa), and conventional antibody Nika102 (150 kDa) were labeled with AlexaFluor680. *In vitro* binding and inhibitory properties of the three AF680 conjugates were assessed by flow cytometry. For *in vivo* imaging experiments, AF680 conjugates were intravenously injected in mice lacking (KO) or overexpressing (TG) ART2. We monitored circulating and excreted AF680 conjugates in plasma and urine and performed *in vivo* near-infrared fluorescence imaging. Nanobody s + 16a^{680} and s + 16mFc^{680} *labeled* and *inhibited* ART2 on T cells in lymph nodes within 10 min. In contrast, mAb Nika102^{680} required 2 h for maximal labeling without inhibition of ART2. *In vivo* imaging revealed specific labeling of ART2-positive lymph nodes but not of ART2-negative lymph nodes with all AF680 conjugates. Even though bivalent s + 16mFc^{680} showed the highest labeling efficiency *in vitro*, the best lymph node imaging *in vivo* was achieved with monovalent nanobody s + 16a^{680}, since renal elimination of unbound s + 16a^{680} significantly reduced background signals. Our results indicate that small single-domain nanobodies are best suited for short-term uses, such as noninvasive imaging, whereas larger nanobody-Fc-fusion proteins are better suited for long-term uses, such as therapy of inflammation and tumors.

Additional supporting information may be found in the online version of this article at the publisher's web site.

Keywords: nanobody; antibody; near-infrared fluorescence imaging; theranostics; T cells

1. INTRODUCTION

An important endeavor in immunobiology is to develop imaging agents that can be used as therapeutic drugs, a concept termed 'theranostics' (1). Monoclonal antibodies are increasingly used for therapy and *in vivo* imaging. However, the use of conventional antibodies for specific noninvasive *in vivo* imaging is limited owing the relatively large size, which impedes tissue penetration and renal elimination (2). Both contribute to suboptimal imaging conditions with low target-to-background ratios (3). Moreover, clinical translation of molecular imaging techniques will require imaging agents with the lowest possible likelihood of toxicity and immunogenicity. One strategy for minimizing these risks is to remove unbound material from the body via renal excretion (4,5).

Nanobodies are small single-domain antigen binding fragments derived from heavy-chain antibodies that are devoid of light chains and occur naturally in camelidae (6,7). With a size of about 13–17 kDa these nanobodies are 10 times smaller than conventional antibodies (150 kDa). Recently, such nanobodies have been shown to enable specific *in vivo* molecular imaging of tumors, inflammation and the biodistribution of specific immune cells (8–13). To the best of our knowledge, there is no description of nanobodies that can be used for *in vivo* near-infrared fluorescence (NIRF) imaging of immune cells and simultaneous

* *Correspondence to: P. Bannas, University Medical Center Hamburg-Eppendorf, Department of Radiology, Martinistrasse 52, 20246 Hamburg, Germany. Email: p.bannas@uke.de*

† *The first two authors contributed equally.*

a *P. Bannas, L. Well, A. Lenz, J. Schmid, G. Adam, H. Ittrich*
Department of Diagnostic and Interventional Radiology, University Medical Center, Hamburg–Eppendorf, Germany

b *L. Well, A. Lenz, B. Rissiek, F. Haag, J. Schmid, F. Koch-Nolte*
Institute of Immunology, University Medical Center, Hamburg-Eppendorf, Germany

c *K. Hochgräfe*
German Center for Neurodegenerative Diseases (DZNE), Bonn, Germany

d *M. Trepel*
Department of Oncology and Hematology, University Medical Center, Hamburg-Eppendorf, Germany

modulation of immune cell function, for example, by inhibition of a specific cell surface enzyme.

Here, we report the use of ADP-ribosyltransferase 2 (ART2) as a model antigen to assess the utility of immunomodulating nanobodies vs conventional antibodies as theranostic tools. Toxin-related ART2 is an ecto-enzyme expressed on murine T cells that catalyzes the transfer of ADP-ribose from NAD^+ onto target proteins on the cell surface, which induces apoptosis of T cells, leading to selective depletion of T cell subsets (14–16). Activity of ART2 can be monitored with the Nicotinamide adenine dinucleotide (NAD)-analog etheno-NAD as substrate and the ethenoadenosine-specific monoclonal antibody 1G4 to detect etheno-ADP-ribosylated proteins on the cell surface (16–18). Recent studies revealed that the activity of ART2 and ART2-mediated selective depletion of T cell subsets can be inhibited by a blocking single-domain nanobody (s + 16a) *in vitro* and *in vivo* (14,19). Moreover, a reformatted nanobody-Fc-fusion protein (s + 16mFc) has been shown to mediate long-term *in vivo* inhibition of ART2 activity and thereby to retard development of autoimmune diabetes in a mouse model (20).

A single nanobody-based probe for noninvasive imaging and simultaneous immunomodulation would be a desirable tool for experimental as well as for clinical applications. In our study, the recently developed ART2-specific monovalent nanobody s + 16a (17 kDa) and the bivalent s + 16mFc-fusion protein (82 kDa) were compared with the conventional monoclonal antibody Nika102 (150 kDa) for their capacity to inhibit and noninvasively image ART2 on T cells using near-infrared-fluorescence imaging *in vivo*.

2. RESULTS

2.1. Labeling and Inhibition of ART2 *in vitro*

Nanobody, nanobody-Fc-fusion protein and conventional antibody were conjugated with AlexaFluor680 (Fig. 1). Flow cytometry revealed specific binding of $s+16a^{680}$, $s+16mFc^{680}$ and $Nika102^{680}$ to ART2 on T cells of BALB/c wild-type (WT) mice and of transgenic mice overexpressing ART2 (TG), but not of ART2-deficient (KO) mice (Fig. 2). The results showed an intermediate level of ART2 on WT T cells and a high level on most, but not all, TG T cells. The monovalent single domain nanobody $s+16a^{680}$ stained T cells slightly less efficiently than the bivalent Fc-fusion protein $s+16mFc^{680}$ and the conventional antibody $Nika102^{680}$. Concomitant monitoring of the enzymatic activity of ART2 with AlexaFluor488-conjugated mAb 1G4 (17) revealed an almost complete inhibition of the enzymatic activity of ART2 on T cells by $s+16a^{680}$ and $s+16mFc^{680}$, but only a slight reduction by mAb $Nika102^{680}$ (Fig. 2b). Control cells from ART2-deficient mice (21) did not show any detectable ART activity, consistent with the lack of ART2 expression on these cells (Fig. 2a, b).

To test the validity of the planned *in vivo* NIRF-imaging experiments we determined the correlation of ART2 staining with flow cytometry and NIRF-imaging (Supporting Information, Fig. 1). Regarding ART2-transfected cells, both techniques showed similar dose-dependent labeling and saturating levels for each of the AF680 conjugates. The two techniques showed a strong correlation ($r = 0.975$). Untransfected cells did not show any detectable signal with Fluorescence activated cell sorting (FACS) or NIRF imaging.

2.2. Labeling and Inhibition of ART2 *in vivo*

T cells from lymph nodes were purified at different time points after injection of 50 μg $s+16a^{680}$, $s+16mFc^{680}$ or $Nika102^{680}$ (corresponding approximately to 3000, 600 and 300 pmol, respectively) and analyzed by flow cytometry for ART2-labeling efficiency. For analysis of ART2-inhibition, T cells were incubated with or without 10 μM etheno-NAD and stained with the etheno-adenosine specific antibody 1G4. Results of *ex vivo* FACS analyses revealed that the smaller constructs $s+16a^{680}$ and $s+16mFc^{680}$ reached maximal labeling of ART2 on lymph node cells within 10 min, whereas the larger mAb $Nika102^{680}$ reached maximal labeling of ART2 only after 2 h (Fig. 3a). Labeling with the bivalent $s+16mFc^{680}$ and $Nika102^{680}$ was constant for 12 h, whereas labeling with monovalent $s+16a^{680}$ declined after 2 h. Consistently, $s+16a^{680}$ and $s+16mFc^{680}$ showed an inhibition of >90% of ART2-activity within 1–2 h (Fig. 3b). Mice injected with $s+16mFc^{680}$ showed persistent inhibition of ART2-activity for 12 h (>90%), whereas inhibition by $s+16a^{680}$ declined to 20% at 12 h after injection. In contrast, mAb $Nika102^{680}$ showed little if any inhibition of ART2-activity. Serum analyses revealed a continuous decline of free $s+16a^{680}$ with an apparent serum half-life of 1–2 h, whereas the larger fusion protein $s+16mFc^{680}$ and mAb $Nika102^{680}$ showed little if any loss from circulation for 12 h (Fig. 3c).

2.3. Serum and Urine Analyses

We performed comparative titration analyses to optimize the concentration of the AF680 conjugates for *in vivo* imaging experiments (Supporting Information, Fig. 2). At 2 h post injection of the highest antibody dose (50 μg), serum samples from both ART2-TG and ART2-KO mice showed high levels of unbound circulating $s+16Fc^{680}$ and $Nika102^{680}$, but little if any unbound $s+16^{680}$ (Supporting Information, Fig. 2a, c). Urine analyses revealed high levels of $s+16a^{680}$, but little if any

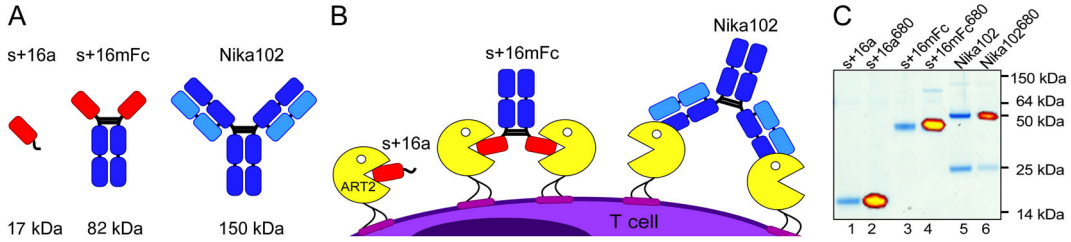

Figure 1. ART2-specific AF680 conjugates. (a) Scheme of nanobody s + 16a, nanobody-Fc-fusion protein s + 16mFc, and mAb Nika102. (b) The deep, NAD^+-binding active site crevice of ART2 is symbolized by the mouth of a 'Pacman'. Both, s + 16a and s + 16mFc block the active site of ART2. Conventional mAb Nika102 binds outside the active site and does not inhibit ART2 activity. (c) Coomassie stained gel overlaid by a corresponding near-infrared fluorescence (NIRF)-image of unconjugated s + 16a, s + 16mFc, and Nika102 (lanes 1, 3 and 5) and respective AF680 conjugates (lanes 2, 4 and 6).

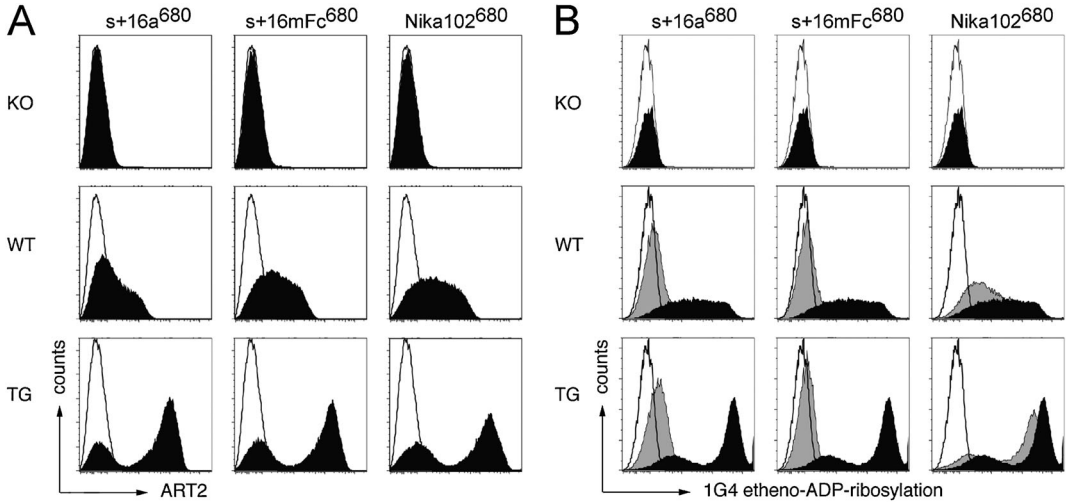

Figure 2. Analyses of ART2-expression and activity. (a) Lymph node cells from ART2-knockout mice (KO), ART2-wild-type mice (WT) and from transgenic mice overexpressing ART2 (TG) were stained with the indicated AF680 conjugates and subjected to FACS analyses. Mean fluorescence intensities of T cells are plotted (solid histograms). Open histograms show isotype controls. (b) Parallel aliquots of cells were pre-incubated in the absence (solid black histograms) or presence (solid gray histograms) of the indicated AF680 conjugates. Cells were then further incubated in the presence of etheno-NAD before detection of etheno-ADP-ribosylated cell surface proteins with mAb 1G4. Control stainings were performed in the absence of etheno-NAD (open histograms). Results are representative of three independent experiments.

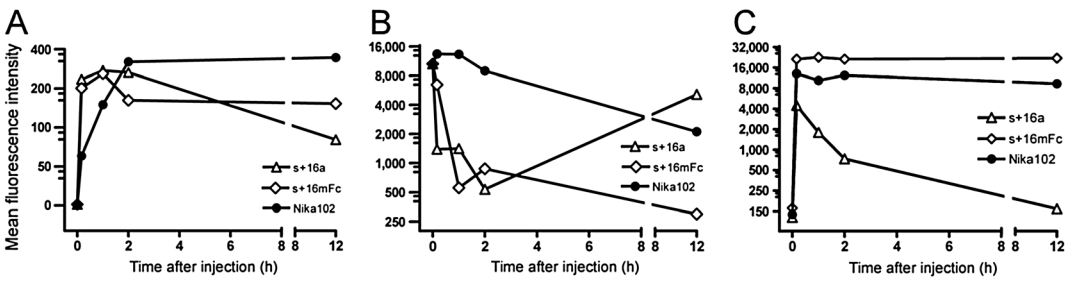

Figure 3. Staining and inhibition of ART2 *in vivo* after injection of AF680 conjugates. Wild-type mice were injected intravenously with 50μg of s + 16a^{680}, s + 16mFc^{680} or Nika102^{680} and sacrificed at the indicated time points. (a) Lymph node cells were subjected to flow cytometry to detect cell surface-bound AF680 conjugates. (b) Parallel aliquots of cells were incubated with 10 μM etheno-NAD for 10 min, washed and stained with 1G4-mAb to monitor ART2 enzyme activity. (c) Serum was analyzed to monitor levels of circulating unbound AF680 conjugates. Results are representative of two independent experiments.

s + 16mFc^{680} and mAb Nika102^{680} (Supporting Information, Fig. 2b, d). At lower doses (5 μg, 0.5 μg), unbound s + 16-Fc and Nika102 were detectable in serum samples of ART2-KO mice, but not in ART2-TG mice.

2.4. *In vivo* NIRF Imaging Experiments

In order to reduce background signals by unbound circulating antibody conjugates, we used 50 μg of s + 16a^{680}, 5 μg of s + 16mFc^{680} and 10 μg of Nika102^{680} (corresponding to 3000, 60 and 60 pmol or 5×10^{14}, 8×10^{13} 6×10^{14} fluorescent dyes per animal, respectively) in these experiments, using the results shown above for guidance. Fluorescence of cervical and axillary lymph nodes was visible in ART2-TG mice after injection of all three conjugates (Fig. 4a). While s + 16mFc^{680} and Nika102^{680} showed strong background fluorescence, there was no background signal in the case of s + 16a^{680}. The clearest images showing high fluorescence of lymph nodes were obtained 2 h post injection of s + 16a^{680} and, in case of the mAb Nika102^{680}, only after 24 h. The Fc-fusion protein s + 16mFc^{680} showed detectable lymph node fluorescence, albeit only slightly above background. Of note, at 24 h after injection of the fusion protein s + 16mFc^{680} and mAb Nika102^{680}, ART2-TG mice showed less diffusely distributed fluorescence than ART2-KO mice. At this time point, none of the mice injected with the s + 16a^{680} showed any detectable background signals.

Semiquantitative analyses of fluorescence intensities of lymph node regions over 24 h confirmed rapid labeling by s + 16a^{680} with a maximal signal 1 h after injection (Fig. 4b). In ART2-KO mice this was followed by a rapid decline in signal intensity. The much slower decline of signal intensity of lymph nodes in ART2-TG mice injected with s + 16a^{680} resulted in high target-to-background ratios from 2 to 24 h.

In contrast, injection of s + 16mFc^{680} and mAb Nika102^{680} yielded maximal lymph node fluorescence only at 2–4 h after injection with signal intensities remaining nearly constant thereafter over 24 h. The lower lymph node signal intensities in mice injected with s + 16mFc^{680} and mAb Nika102^{680} vs s + 16a^{680} are consistent with the amounts of injected conjugates. Labeling of TG lymph nodes was clear and distinguishable

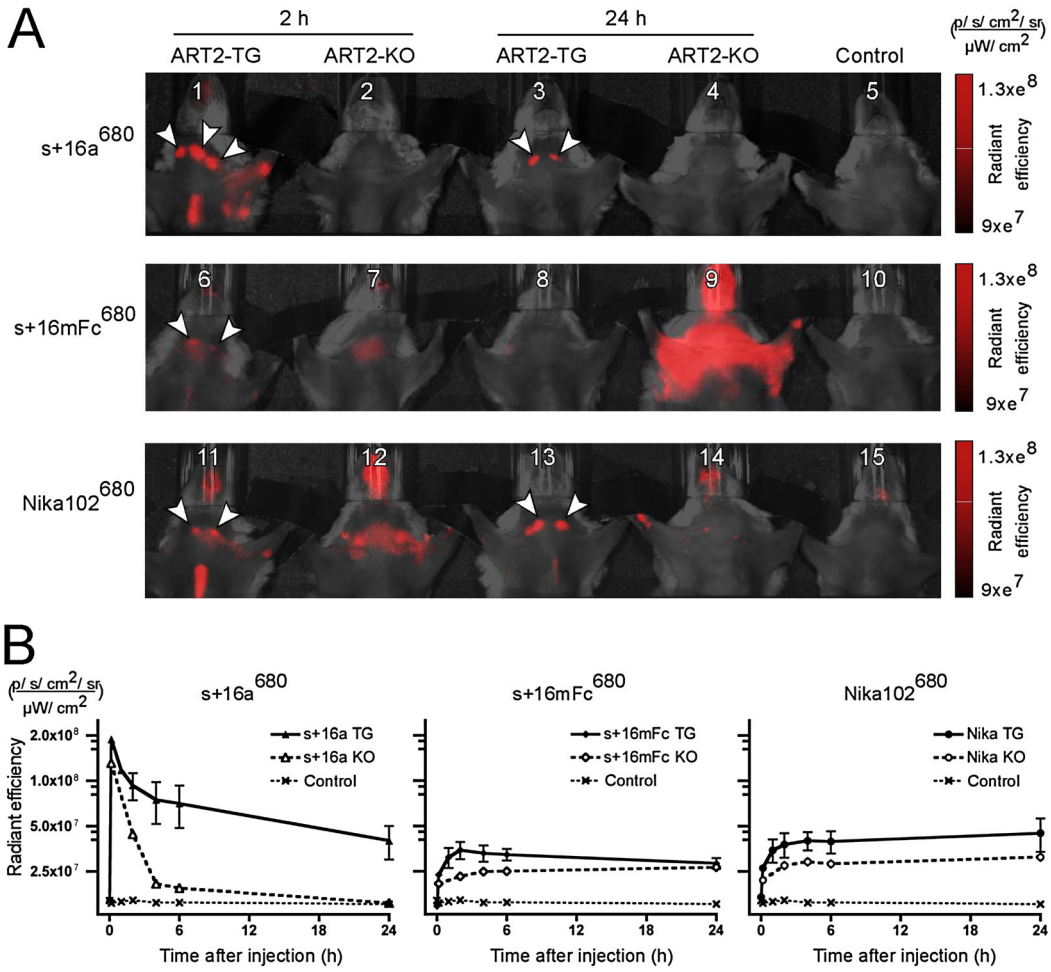

Figure 4. *In vivo* NIRF-imaging. (a) ART2-TG mice and ART2-KO mice were injected with buffer (control), 50 µg s + 16a^{680}, 5 µg s + 16mFc^{680} or 10 µg Nika102^{680}. Groups of control and antibody-injected mice (2 and 24 h after injection) were then subjected to simultaneous NIRF imaging to obtain visually comparable images. Arrowheads indicate cervical and axillary lymph nodes. (b) Radiant efficiencies of regions of interest of lymph nodes are plotted as a function of time for control mice and mice injected with s + 16a^{680}, s + 16mFc^{680} and Nika102^{680}. Data are presented as means ± SD from four independent experiments.

compared to KO lymph nodes for all AF680 conjugates at all imaging time points. However, the difference in labeling intensity of TG vs KO lymph nodes was far higher for s + 16a^{680} than for the larger conjugates s + 16mFc^{680} and Nika102^{680} for the entire period from 2 to 24 h.

2.5. *Ex vivo* NIRF Imaging Experiments

In order to evaluate whether and to what extent the diffuse fluorescence observed (stronger in ART2-KO than in ART2-TG mice) after injection of the larger AF680 conjugates is attributed to unbound circulating antibodies, serum samples were analyzed for the presence of free AF680 conjugates at the time of sacrifice (Supporting Information, Fig. 3a, b). The results revealed higher levels of unbound s + 16mFc^{680} and mAb Nika102^{680} in ART2-KO than in ART2-TG mice already 2 h after injection (Supporting Information, Fig. 3 a). At 24 h after injection, no detectable unbound AF680 conjugates remained in ART2-TG mice, while ART2-KO mice still showed high levels of unbound s + 16mFc^{680} and Nika102^{680} (Supporting Information, Fig. 3 b). Concomitant analyses of urine samples revealed that renal excretion of s + 16a^{680} is terminated 24 h after injection (Supporting Information, Fig. 3, compare c and d).

To further validate the *in vivo* NIRF-imaging data, harvested lymph nodes were imaged *ex vivo* (Fig. 5). *Ex vivo* NIRF-imaging of isolated lymph nodes (Fig. 5a) confirmed specific labeling of cervical and axillary lymph nodes in ART2-TG mice but not in ART2-KO mice with all conjugates. Fluorescence intensities of lymph nodes obtained from ART2-TG mice injected with s + 16a^{680} were 5–13 times higher than those from mice injected with s + 16mFc^{680} and Nika102^{680} (Fig. 5b, Table 1). The results confirm the decline of lymph node fluorescence 24 h after injection of s + 16a-AF680, whereas lymph node fluorescence from ART2-TG mice remained constant from 2 to 24 h after injection of the larger AF680 conjugates (Fig. 5b, Table 1). At 2 h after injection all three AF680 conjugates showed significant differences in lymph node signals from ART2-TG and ART2-KO mice, whereas after 24 h only s + 16a^{680} and Nika102^{680} still showed significant differences.

Analyses of spleen, lung, liver, kidneys, stomach and muscle tissue (Table 1) showed that signals from spleen reflect those described above for lymph nodes with significant

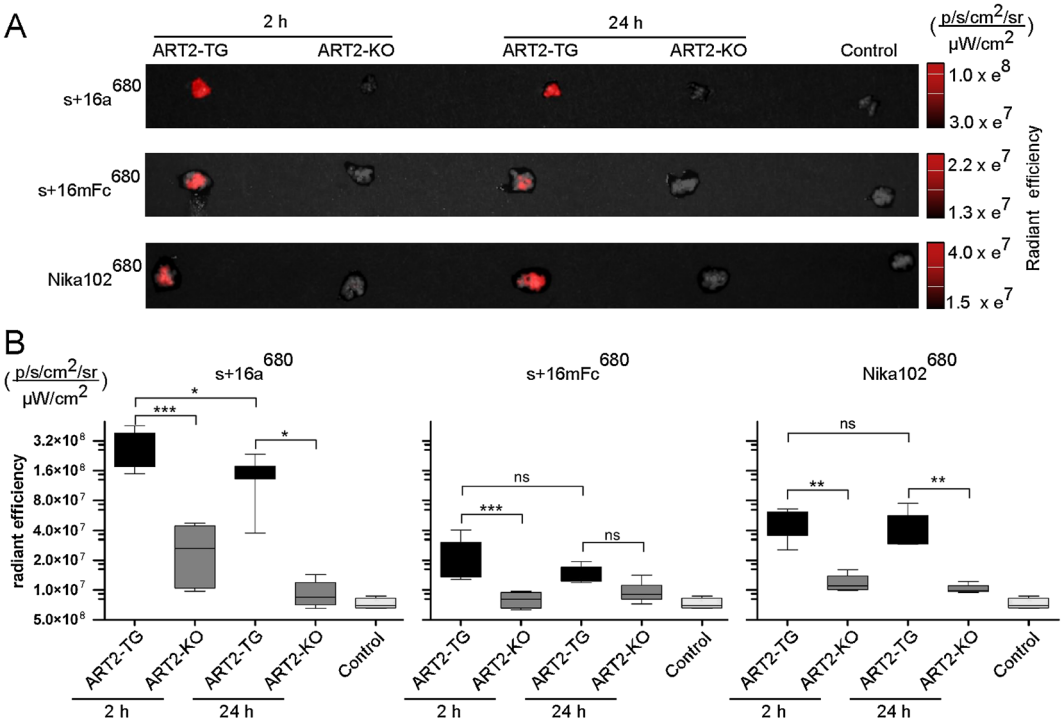

Figure 5. *Ex vivo* NIRF-imaging. (a) In order to quantitate lymph node associated fluorescence in the absence of potentially confounding signals from other tissues, lymph nodes (four axillary, two cervical and two inguinal) were dissected and pooled for direct NIRF-imaging. (b) Radiant efficiencies of pooled lymph nodes are presented as means ± SD from four independent experiments.

Table 1. *Ex vivo* radiant efficiencies of individual organs. Radiant effects ($\times 10^{10}$) are presented as means ± SD. Statistical analyses were performed using one-way ANOVA and Bonferroni post tests. n.s., Not significant. *p*-Values are given for results of organs from ART2-transgenic (TG) vs ART2-knockout (KO) mice

Time point	Construct	Animals	Lymph nodes	Spleen	Lung	Liver	Kidneys	Stomach	Muscle
2 h p.i.	**s + 16a**	**TG**	27.9 ± 6.7	17.0 ± 2.5	6.4 ± 1.2	34.4 ± 3.4	432.3 ± 63.8	17.9 ± 4.1	2.5 ± 0.6
		KO	2.8 ± 1.0	1.2 ± 0.2	2.9 ± 0.6	13.6 ± 3.3	406.0 ± 20.4	13.4 ± 4.6	1.0 ± 0.2
		p	<0.001	<0.001	<0.01	<0.001	n.s.	n.s.	<0.05
	s + 16mFc	**TG**	2.11 ± 0.4	5.8 ± 1.3	2.3 ± 0.2	8.7 ± 1.7	3.0 ± 0.4	19.0 ± 10.2	0.6 ± 0.1
		KO	0.8 ± 0.1	1.2 ± 0.1	1.6 ± 0.1	7.2 ± 1.0	2.4 ± 0.2	4.0 ± 0.3	0.7 ± 0.4
		p	<0.001	<0.001	<0.01	n.s.	n.s.	n.s.	n.s.
	Nika102	**TG**	4.9 ± 0.9	11.6 ± 2.1	2.9 ± 0.5	6.7 ± 0.9	2.8 ± 0.3	4.9 ± 0.2	0.7 ± 0.1
		KO	1.2 ± 0.1	1.4 ± 0.1	3.8 ± 0.4	10.4 ± 2.1	4.0 ± 0.5	4.9 ± 0.3	0.9 ± 0.1
		p	<0.01	<0.001	n.s.	n.s.	<0.05	n.s.	n.s.
24 h p.i.	**s + 16a**	**TG**	15.0 ± 2.3	6.1 ± 1.0	1.8 ± 0.3	3.2 ± 0.3	10.6 ± 2.4	5.3 ± 0.8	0.7± 0.1
		KO	0.9 ± 0.2	1.0 ± 0.1	1.0 ± 0.1	2.5 ± 0.5	12.4 ± 7.1	4.4 ± 1.1	0.9 ± 0.1
		p	<0.05	<0.05	n.s.	n.s.	n.s.	n.s.	n.s.
	s + 16mFc	**TG**	1.5 ± 0.1	1.5 ± 0.1	1.1 ± 0.1	1.7 ± 0.1	1.3 ± 0.1	3.1 ± 0.2	0.6 ± 0.4
		KO	1.0 ± 0.1	0.9 ± 0.1	1.6 ± 0.2	3.5 ± 0.7	1.9 ± 0.2	4.7 ± 0.7	0.7 ± 0.3
		p	n.s.	n.s.	n.s.	n.s.	n.s.	n.s.	n.s.
	Nika102	**TG**	3.9 ± 0.7	5.5 ± 0.7	1.3 ± 0.1	1.7 ± 0.1	1.4 ± 0.1	2.7 ± 0.2	0.6 ± 0.1
		KO	1.0 ± 0.1	0.8 ± 0.1	1.7 ± 0.1	2.9 ± 0.4	2.0 ± 0.1	3.7 ± 0.5	0.7 ± 0.1
		p	<0.01	<0.01	n.s.	n.s.	n.s.	n.s.	n.s.

differences in fluorescence signals between ART2-TG and ART2-KO mice after 2 h for all three AF680 conjugates. Lung, liver and muscle showed significant differences in fluorescence only at 2 h after injection of s + 16a^{680}. At 24 h after injection of s + 16a^{680} and Nika102^{680}, lung, liver, kidney, stomach and muscle organs from ART2-TG vs ART2-KO mice did not show any significant differences in fluorescence while lymph nodes and spleen (Table 1) still showed significant differences. Highest signal intensity was observed in kidneys 2 h after injection of s + 16a^{680}.

3. DISCUSSION

In this study we report that simultaneous immunomodulation and molecular imaging of T cells *in vivo* is achievable with nanobodies. We used AF680-conjugated nanobodies to link *in vivo* analyses by NIRF-imaging to *ex vivo* cell discriminating assays by flow cytometry. Our results demonstrate that monovalent s + 16a^{680} and bivalent s + 16mFc^{680} allow specific labeling and inhibition of ART2 on T cells *in vitro* and *in vivo*. Even though s + 16mFc^{680} had the highest labeling efficiency *in vitro*, best lymph node imaging *in vivo* was achieved with nanobody s + 16a^{680}.

Specific labeling and imaging of cells with antibody conjugates directed against cell surface proteins is more challenging *in vivo* than *in vitro*. *In vitro*, conjugates have direct access to their target cells and excess conjugates can readily be removed by washing cells, yielding highly specific signals. *In vivo*, conjugates need to cross barriers to reach their target and unbound conjugates cause background signals until they are removed from the system, for example, by renal or biliary excretion (4,5). Our results indicate that the format of an antibody conjugate governs its capacity to cross barriers and its removal from the system, thereby profoundly affecting the signal-to-background ratio and the optimal time point for *in vivo* imaging.

An ideal targeted imaging agent should be able to penetrate the tissue, bind to specific cell surface antigens with sufficient affinity to be retained in the target tissue and to be cleared rapidly from the circulation to enable imaging in a reasonable timescale (4,5). The rapid renal clearance of s + 16a^{680} allowed us to use high concentrations of s + 16a (50 μg or 3000 pmol) for *in vivo* NIRF-imaging experiments. Comparative analyses of unbound conjugates in sera of ART2KO and ART2TG mice allowed us to adjust the dosage of bivalent s + 16mFc (5 μg or 60 pmol) and Nika102 (10 μg or 60 pmol) conjugates to minimize levels of circulating antibodies while still permitting good staining of lymph node cells. To assess potential retention and metabolism of A680 conjugates by other organs, we performed region of interest (ROI)-based quantification from isolated organs. The results revealed the highest signal in kidneys of mice 2 h after injection of s + 16a^{680}, reflecting its renal excretion. Relatively high signals were also observed in the spleen of ART2-transgenic but not ART2-deficient mice, consistent with the high content of ART2^{+} T cells in the spleen. Signals from the liver in both ART2-transgenic and ART2-deficient mice could be due to partial biliary elimination of AF680 conjugates and depleted fluorescent dye alone.

Our results are in accordance with previous studies, where large, intact IgG antibody molecules with proven therapeutic benefit demonstrated limited utility in molecular imaging owing to their slow clearance from circulation and tissues, resulting in limited imaging contrast early after injection owing to a high background signal (2). This limitation can be overcome by engineering antibody fragments (nanobodies) that retain specific binding to the target antigen and at the same time achieve fast blood clearance (9,12). It is conceivable that imaging of ART2 + cells could be enhanced further via dimerization of the nanobody, for example, by genetic fusion or by disulfide linkages, which could enhance the avidity of the probe for the target cells while at the same time retaining elimination via the kidney. While these nanobodies are ideally suited for imaging applications, their rapid renal elimination limits their use for long-term therapeutic applications. To this end it would be desirable to increase their apparent size to over 65 kDa to bypass kidney filtration (20,22). This can be achieved by various antibody engineering strategies, such as, multimerization, fusion to other antibody fragments or creation of bi-specific sdAbs, where one fragment binds to a plasma carrier, such as albumin, to increase the serum half-life (20,22–25). In accord with a previous study (20), increasing the size by fusing the nanobody s + 16a to the Fc domain of murine IgG1 improved and prolonged the immunomodulatory properties *in vivo*. Inhibition of ART2 by s + 16a protects regulatory T cells and iNKT cells from acute NAD-induced cell death, whereas s + 16-Fc provides persistent protection (14,20). It will be interesting to determine whether the imaging techniques presented here will be theranostically useful in models of acute inflammatory reactions such as ConA-induced hepatits (26) and chronic inflammatory reactions such as autoimmune diabetes (20).

An inherent technical limitation of NIRF-imaging is its low penetration depth of 7–10 mm owing to the absorbance and scattering of light within biological tissues, resulting in lower sensitivities than radioimmunological methods. Currently, these limitations are addressed by the development of tomographic photo-acoustic techniques allowing whole-body imaging of living mice (27). Besides these limitations, NIRF-imaging provides several advantages compared with other established pre-clinical imaging techniques, such as computed tomography, magnetic resonance imaging, and nuclear imaging (3,28). NIRF imaging is nonradioactive, highly sensitive and relatively inexpensive, and the targeted probes are comparatively easy to produce and store (29,30). Our results demonstrated that NIRF-conjugated nanobodies have excellent properties for rapid preclinical optical imaging, which holds promise for their future use as diagnostic tools in humans. Moreover, the presented NIRF imaging techniques can be easily translated to immuno-PET (Positron emission tomography) imaging by radiolabeling of nanobodies. A recent PET study confirmed faster kinetics of radiolabeled nanobodies, allowing high contrast imaging at early time points in comparison with radiolabeled conventional monoclonal antibodies (12). Also the therapeutic aspects of nanobodies have been highlighted in a recent study, where radiolabeled nanobodies have been modified to extend their serum half-life for optimized tumor therapy (25).

4. CONCLUSIONS

In this study we illustrated NIRF-imaging with nanobodies as a powerful tool to detect immune cells *in vivo* and to simultaneously modulate their function, highlighting the potential utility of nanobodies as theranostics. The techniques described here may serve as a model for other nanobody-based applications: small single domain nanobodies are best suited for short-term uses, for example, noninvasive imaging, whereas larger nanobody-Fc-fusion proteins are better suited for long-term uses, for example, therapy of inflammation and tumors.

5. EXPERIMENTAL

5.1. Chemicals, Cells and Mice

Etheno-NAD was obtained from Sigma-Aldrich. Phycoerythrin (PE)- and Fluorescein isothiocyanate (FITC)-conjugated monoclonal

antibodies were purchased from BD Pharmingen. Mouse monoclonal antibody 1G4 (17) was conjugated to fluorochrome Alexa488 as described previously (18). Untransfected and ART2-transfected DC27.10 mouse lymphoma cells were cultured as described previously (16). BALB/c wild-type mice were obtained from the Jackson Laboratory. Generation of ART2-deficient mice and of transgenic mice with overexpression of ART2 on T cells was described previously (21,31). Animal experiments were performed in accordance with international guidelines on the ethical use of animals and were approved by the local animal welfare commission.

5.2. Generation of ART2-Specific AF680 Conjugates

Generation and purification of nanobody s + 16a (19), Fc-Fusion protein s + 16mFc (20) and of monoclonal antibody Nika102 (32) were described previously. ART2 specific probes were conjugated by random reaction of primary amines to the succinimidyl ester moiety of fluorescent dye AlexaFluor-680 (AF680) (excitation wavelength 679 nm, emission wavelength 702 nm). The numbers of dye molecules per probe (0.3, 1.2 and 2.0 for s + 16a, s + 16mFc and Nika102, respectively) were calculated according to the manufacturer's instructions (Molecular Probes; using molar extinction coefficients of 15 720, 51 170 and 203 000 $mol^{-1}\,cm^{-1}$, respectively). Purity of antibody constructs before and after conjugation to AF680 was assessed by SDS–PAGE size fractionation and Coomassie Brilliant Blue gel stain (Fig 1). Binding affinities before and after conjugation as well as stability during overnight incubation at 37 °C in serum were assessed by serial dilution of probes and flow cytometry of DC27.10 cells. Binding affinities were 10 nM for Nika102, 5 nM for s + 16mFc and 40 nM for s + 16a. The results showed less than 10% reduction in labeling efficiencies (mean fluorescent intensity) upon conjugation and overnight incubation in serum (results not shown).

5.3. Analysis of ART2 Expression and Enzymatic Activity

Mice were sacrificed by exposure to O_2/CO_2 followed by cervical dislocation. Single-cell suspensions were prepared from lymph nodes as described previously (31). For ART2-expression analyses, cells (1×10^6) were stained with s + 16a, s + 16mFc and Nika102 AF680 conjugates (1 μg ml^{-1}) or AF680-control antibodies and counterstained with PE-anti-CD3 for 20 min at 4 °C.

For ART2-activity analyses, cells (1×10^6) were pre-incubated in the presence or absence of s + 16a, s + 16mFc and Nika102 AF680 conjugates (1 μg ml^{-1}) and then with or without 1 μM etheno-NAD for 20 min at 4 °C. Cells were washed twice and stained with ethenoadenosine-specific mAb Alexa488-1G4 (1 μg ml^{-1}) and counterstained with PE-anti-CD3. Cells were washed twice and analyzed by flow cytometry on FACSCantoII. Dead cells were excluded after staining with propidium iodide.

5.4. *In vitro* NIRF Imaging

An aliquot of 1.1×10^7 of untransfected or ART2-transfected DC27.10 cells was incubated with different concentrations of $s+16a^{680}$, $s+16mFc^{680}$ or $Nika102^{680}$ for 30 min at 4 °C and washed twice. An aliquot of 1×10^7 cells was sedimented on a black 96-well plate (Nunc). Measurements were performed with a whole-body small-animal NIRF imaging system (IVIS-Spectrum, Caliper LifeSciences) using the 675 nm band-pass (30 nm bandwidth) filter for excitation and the 720, 740, 760 and 780 nm band-pass filters (20 nm bandwidth) for emission with a 512×512 pixel matrix size (15×15 μm per pixel). Images were analyzed semi-quantitatively by placing a ROI on individual wells. Total radiant efficiency was calculated with Living Image 4.2 software (Caliper LifeSciences). An aliquot of 1×10^6 cells was subjected to flow cytometry for comparative analysis.

5.5. Analyses of AF680 Conjugates After Intravenous Injection

An aliquot of 50 μg of $s+16a^{680}$, $s+16mFc^{680}$ or $Nika102^{680}$ (corresponding to approximately 3000, 600 and 300 pmol, respectively) in a volume of 200 μl was administered intravenously into BALB/c wild-type mice. T cells from lymph nodes were purified at different time points after injection. For flow cytometric analysis of ART2-labeling efficiency, purified T cells were counterstained with PE-anti-CD3. For analysis of ART2-inhibition by the different AF680 conjugates, T cells were incubated with or without 10 μM etheno-NAD, washed twice and stained with Alexa488-1G4 and PE-anti-CD3.

To measure blood clearance and renal excretion of AF680 conjugates, mice were sacrificed at different time points post injection and blood and urine were collected. AF680 conjugates were quantified by flow cytometry using serum (1:100 dilution) and urine (1:100 dilution) in a total volume of 100 μl for labeling 1×10^6 ART2-expressing DC27.10 cells. For assessment of optimal *in vivo* imaging conditions, AF680 conjugate concentrations of 0.5, 5 or 50 μg of $s+16a^{680}$, $s+16mFc^{680}$and $Nika102^{680}$ were injected intravenously into wild-type mice. Animals were sacrificed at different time points after injection and free abundant AF680 conjugates in serum and urine were quantified as described above.

5.6. *In vivo* and *ex vivo* NIRF Imaging

ART2-deficient and ART2-overexpressing mice were maintained on an alfalfa-free diet for 2 weeks prior to imaging experiments. The day prior to the imaging experiment the ventral and lateral throat, thorax and abdomen were depilated. For imaging experiments 50 μg $s+16a^{680}$, 5 μg $s+16mFc^{680}$ and 10 μg of $Nika102^{680}$ (corresponding to approximately 3000, 60 and 60 pmol, respectively) were administered intravenously in a volume of 200 μl. Mice were anesthetized with isofluorane and positioned in the imaging chamber, allowing for maintenance of gaseous anesthesia. NIRF-imaging was performed before and 10 min and 1, 2, 4, 6 and 24 h after injection. Imaging parameters were the same as for *in vitro* imaging experiments. Radiant efficiency was estimated using manually drawn ROIs around the four brightest cervical and axillary lymph node regions.

To validate the *in vivo* data, animals were sacrificed 2 or 24 h after injection. NIRF imaging was performed of harvested lymph nodes, spleens, lungs, livers, kidneys, muscle tissue and stomachs, and radiant efficiencies were estimated.

5.7. Statistical Analysis

To assess the validity of semiquantitative results from NIRF imaging, radiant efficiency measurements from NIRF imaging *in vitro* experiments were compared with mean fluorescence intensities from flow cytometry using Pearson's correlation coefficient. All presented radiant efficiency data were calculated from four independent experiments. A one-way ANOVA with a subsequent Bonferroni *post hoc* analysis was used to determine significant differences between measurements obtained at different time points and between measurements obtained from ART2-expressing and ART2-deficient animals. A value of $p < 0.05$ indicates statistical significance. Data are presented as means ± standard deviations. Statistical analysis was performed using Prism 4 for Macintosh and Excel, Microsoft.

Acknowledgments

Parts of this work represent partial fulfillment of the requirements for the graduate thesis of Lennart Well and Alexander Lenz at the University Hospital, Hamburg. This work was supported by the Werner-Otto-Foundation (Peter Bannas) and by the Wilhelm-Sander-Foundation (Peter Bannas and Friedrich Koch-Nolte). We thank Valentin Kunick for critical reading of the manuscript.

REFERENCES

1. Lee DY, Li KC. Molecular theranostics: a primer for the imaging professional. Am J Roentgenol 2011; 197(2): 318–324.
2. Lisy MR, Goermar A, Thomas C, Pauli J, Resch-Genger U, Kaiser WA, Hilger I. *In vivo* near-infrared fluorescence imaging of carcinoembryonic antigen-expressing tumor cells in mice. Radiology 2008; 247(3): 779–787.
3. Frangioni JV. New technologies for human cancer imaging. J Clin Oncol 2008; 26(24): 4012–4021.
4. Choi HS, Liu W, Liu F, Nasr K, Misra P, Bawendi MG, Frangioni JV. Design considerations for tumour-targeted nanoparticles. Nat Nanotechnol 2010; 5(1): 42–47.
5. Choi HS, Liu W, Misra P, Tanaka E, Zimmer JP, Itty Ipe B, Bawendi MG, Frangioni JV. Renal clearance of quantum dots. Nat Biotechnol 2007; 25(10): 1165–1170.
6. Hamers-Casterman C, Atarhouch T, Muyldermans S, Robinson G, Hamers C, Songa EB, Bendahman N, Hamers R. Naturally occurring antibodies devoid of light chains. Nature 1993; 363(6428): 446–448.
7. Wesolowski J, Alzogaray V, Reyelt J, Unger M, Juarez K, Urrutia M, Cauerhff A, Danquah W, Rissiek B, Scheuplein F, Schwarz N, Adriouch S, Boyer O, Seman M, Licea A, Serreze DV, Goldbaum FA, Haag F, Koch-Nolte F. Single domain antibodies: promising experimental and therapeutic tools in infection and immunity. Med Microbiol Immunol 2009; 198(3): 157–174.
8. Zaman MB, Baral TN, Jakubek ZJ, Zhang J, Wu X, Lai E, Whitfield D, Yu K. Single-domain antibody bioconjugated near-IR quantum dots for targeted cellular imaging of pancreatic cancer. J Nanosci Nanotechnol 2011; 11(5): 3757–3763.
9. De Groeve K, Deschacht N, De Koninck C, Caveliers V, Lahoutte T, Devoogdt N, Muyldermans S, De Baetselier P, Raes G. Nanobodies as tools for *in vivo* imaging of specific immune cell types. J Nucl Med 2010; 51(5): 782–789.
10. Tchouate Gainkam LO, Keyaerts M, Caveliers V, Devoogdt N, Vanhove C, Van Grunsven L, Muyldermans S, Lahoutte T. Correlation between epidermal growth factor receptor-specific nanobody uptake and tumor burden: a tool for noninvasive monitoring of tumor response to therapy. Mol Imag Biol 2011; 13(5): 940–948.
11. Ta HT, Prabhu S, Leitner E, Jia F, von Elverfeldt D, Jackson K, Heidt T, Nair A, Pearce H, von Zur Muhlen C, Wang X, Peter K, Hagemeyer CE. Enzymatic single-chain antibody tagging: a universal approach to targeted molecular imaging and cell homing in cardiovascular disease. Circul Res 2011; 109(4): 365–373.
12. Vosjan MJ, Perk LR, Roovers RC, Visser GW, Stigter-van Walsum M, van Bergen En Henegouwen PM, van Dongen GA. Facile labelling of an anti-epidermal growth factor receptor Nanobody with 68Ga via a novel bifunctional desferal chelate for immuno-PET. Eur J Nucl Med Mol Imag 2011; 38(4): 753–763.
13. Oliveira S, van Dongen GA, Stigter-van Walsum M, Roovers RC, Stam JC, Mali W, van Diest PJ, van Bergen en Henegouwen PM. Rapid visualization of human tumor xenografts through optical imaging with a near-infrared fluorescent anti- epidermal growth factor receptor nanobody. Mol Imag Biol 2012; 11(1): 33–46.
14. Hubert S, Rissiek B, Klages K, Huehn J, Sparwasser T, Haag F, Koch-Nolte F, Boyer O, Seman M, Adriouch S. Extracellular NAD+ shapes the Foxp3+ regulatory T cell compartment through the ART2-P2X7 pathway. J Exp Med 2010; 207(12): 2561–2568.
15. Seman M, Adriouch S, Scheuplein F, Krebs C, Freese D, Glowacki G, Deterre P, Haag F, Koch-Nolte F. NAD-induced T cell death: ADP-ribosylation of cell surface proteins by ART2 activates the cytolytic P2X7 purinoceptor. Immunity 2003; 19(4): 571–582.
16. Bannas P, Adriouch S, Kahl S, Braasch F, Haag F, Koch-Nolte F. Activity and specificity of toxin-related mouse T cell ecto-ADP-ribosyltransferase ART2.2 depends on its association with lipid rafts. Blood 2005; 105(9): 3663–3670.
17. Krebs C, Koestner W, Nissen M, Welge V, Parusel I, Malavasi F, Leiter EH, Santella RM, Haag F, Koch-Nolte F. Flow cytometric and immunoblot assays for cell surface ADP-ribosylation using a monoclonal antibody specific for ethenoadenosine. Anal Biochem 2003; 314(1): 108–115.
18. Bannas P, Graumann O, Balcerak P, Peldschus K, Kaul MG, Hohenberg H, Haag F, Adam G, Ittrich H, Koch-Nolte F. Quantitative magnetic resonance imaging of enzyme activity on the cell surface: in vitro and *in vivo* monitoring of ADP-ribosyltransferase 2 on T cells. Mol Imag 2010; 9(4): 211–222.
19. Koch-Nolte F, Reyelt J, Schossow B, Schwarz N, Scheuplein F, Rothenburg S, Haag F, Alzogaray V, Cauerhff A, Goldbaum FA. Single domain antibodies from llama effectively and specifically block T cell ecto-ADP-ribosyltransferase ART2.2 *in vivo*. FASEB J 2007; 21(13): 3490–3498.
20. Scheuplein F, Rissiek B, Driver JP, Chen YG, Koch-Nolte F, Serreze DV. A recombinant heavy chain antibody approach blocks ART2 mediated deletion of an iNKT cell population that upon activation inhibits autoimmune diabetes. J Autoimmun 2010; 34(2): 145–154.
21. Ohlrogge W, Haag F, Lohler J, Seman M, Littman DR, Killeen N, Koch-Nolte F. Generation and characterization of ecto-ADP-ribosyltransferase ART2.1/ART2.2-deficient mice. Mol Cell Biol 2002; 22(21): 7535–7542.
22. Iqbal U, Trojahn U, Albaghdadi H, Zhang J, O'Connor-McCourt M, Stanimirovic D, Tomanek B, Sutherland G, Abulrob A. Kinetic analysis of novel mono- and multivalent VHH-fragments and their application for molecular imaging of brain tumours. Br J Pharmacol 2010; 160(4): 1016–1028.
23. Roovers RC, van Dongen GA, van Bergen en Henegouwen PM. Nanobodies in therapeutic applications. Curr Opin Mol Ther 2007; 9(4): 327–335.
24. Vosjan MJ, Vercammen J, Kolkman JA, Stigter-van Walsum M, Revets H, van Dongen GA. Nanobodies targeting the hepatocyte growth factor: potential new drugs for molecular cancer therapy. Mol Cancer Ther 2012; 11(4): 1017–1025.
25. Roovers RC, Vosjan MJ, Laeremans T, El Khoulati R, de Bruin RC, Ferguson KM, Verkleij AJ, van Dongen GA, van Bergen En Henegouwen PM. A biparatopic anti-EGFR nanobody efficiently inhibits solid tumour growth. Int J Cancer 2011; 129(8): 2013–2024.
26. Kawamura H, Aswad F, Minagawa M, Govindarajan S, Dennert G. P2X7 receptors regulate NKT cells in autoimmune hepatitis. J Immunol 2006; 176(4): 2152–2160.
27. Razansky D, Buehler A, Ntziachristos V. Volumetric real-time multispectral optoacoustic tomography of biomarkers. Nat Protoc 2011; 6(8): 1121–1129.
28. Hoffman JM, Gambhir SS. Molecular imaging: the vision and opportunity for radiology in the future. Radiology 2007; 244(1): 39–47.
29. Hamada Y, Gonda K, Takeda M, Sato A, Watanabe M, Yambe T, Satomi S, Ohuchi N. *In vivo* imaging of the molecular distribution of the VEGF receptor during angiogenesis in a mouse model of ischemia. Blood 2011; 118(13): e93–e100.
30. Weissleder R, Ntziachristos V. Shedding light onto live molecular targets. Nat Med 2003; 9(1): 123–128.
31. Bannas P, Scheuplein F, Well L, Hermans-Borgmeyer I, Haag F, Koch-Nolte F. Transgenic overexpression of toxin-related ecto-ADP-ribosyltransferase ART2.2 sensitizes T cells but not B cells to NAD-induced cell death. Mol Immunol 2011; 48(15–16): 1762–1770.
32. Koch-Nolte F, Duffy T, Nissen M, Kahl S, Killeen N, Ablamunits V, Haag F, Leiter EH. A new monoclonal antibody detects a developmentally regulated mouse ecto-ADP-ribosyltransferase on T cells: subset distribution, inbred strain variation, and modulation upon T cell activation. J Immunol 1999; 163(11): 6014–6022.

Supporting information

Additional supporting information may be found in the online version of this article at the publisher's web site.